## Title

# Surface crosslinking of virus-like particles increases resistance to proteases, low pH, and mechanical stress for mucosal applications

## Authors & Affiliations

Ahmed Ali [a], Suwannee Ganguillet [a], Yagmur Turgay [a], Tim Keys [a], Erika Causa [b], Ricardo Fradique [b], Viviane Lutz-Bueno [c,d], Serge Chesnov [e], Chia-wei Lin [e], Verena Lentsch [a], Jurij Kotar [b], Pietro Cicuta [b], Raffaele Mezzenga [a], Emma Slack [a,*], Milad Radiom [a,c,*]

[a] Institute of Food, Nutrition and Health, ETH Zürich, Zürich, Switzerland
[b] Biological and Soft Systems, Cavendish Laboratory, University of Cambridge, Cambridge CB3 0HE, U.K.
[c] Paul Scherrer Institute PSI, Villigen, Switzerland
[d] Laboratoire Léon Brillouin, CEA-CNRS (UMR-12), CEA Saclay, Université Paris-Saclay, 91191, Gif-sur-Yvette Cedex, France
[e] University of Zürich/ETH Zürich, Functional Genomics Centre Zürich, Zürich, Switzerland

*Milad Radiom (milad.radiom@hest.ethz.ch); Emma Slack (emma.slack@hest.ethz.ch)

## Abstract

Virus-like particles (VLPs) are emerging as nano-scaffolds in a variety of biomedical applications including the delivery of vaccine antigens to mucosal surfaces. These soft, colloidal, and proteinaceous structures (capsids) are nevertheless susceptible to mucosal environmental factors which limit their usefulness. We addressed this issue by crosslinking multiple capsid surface reactive residues using polyethylene glycol tethers. Surface crosslinking enhanced the colloidal stability and mechanical strength of VLPs against low pH, proteases, and mechanical agitation, while it did not interfere with function as vaccine. Chemical crosslinking thus offers a viable means to enhance the resilience of VLPs in mucosal applications.



## Keywords

Virus-like particle; Polyethylene glycol; Surface-crosslinking; Force spectroscopy; In vitro human nasal epithelial tissue; Mucus

# Introduction

Virus-like particles (VLPs) have emerged as invaluable nano-carriers in biomedical applications (*1, 2*). Sensitive cargo can be protected by packaging it inside their capsid while genetic and/or chemical modifications can be used to deliver vaccine antigens or to target the cargo to specific cell types. In recent years, various therapeutic molecules have been integrated into VLPs for immunotherapy (*3*), gene therapy (*4-6*), chemotherapy (*7-9*), as well as for contrast imaging and photothermal therapy (*10, 11*).

As carriers, VLPs must endure environmental challenges and it is likely that their material properties are an important factor determining their fate (*12*). General key considerations for “delivery-capable” VLPs include size, colloidal stability, target specificity, and responsiveness to stimuli for cargo release. For mucosal applications, VLPs are faced with additional physiological challenges including a thick and adhesive mucus gel, mucus regeneration and clearance, high concentrations of proteases and secretory immunoglobulin A (sIgA) antibodies and intermittent mechanical agitation (*13-15*). Together these effects can significantly reduce the efficacy of VLPs for mucosal applications (**Figure 1**(a)).

To this end, there is compelling evidence that viruses, viral vectors, and VLPs disintegrate under mechanical force (*16-25*), and in unfavorable chemical environments (*26, 27*). This raised the question: can surface crosslinking using macromolecule tethers enhance the stability of VLP capsids? To address this question, we employed homobifunctional polyethylene glycol (PEG) to tether surface lysine residues on capsid surface. VLP or viral vector PEGylation, without crosslinking, has been exploited as a means to enhance biological function, especially with adenovirus vectors (Adv). For example, PEGylation protected Adv from neutralizing antibodies, prolonged transgene expression and reduced immune activation against the vector (*28-30*). Subsequent experiments revealed a complex dependence on bio-physicochemical properties (*31-33*). Thereby, for example, conjugation optimization led to reduced anti-vector serum antibody and more persistent transgene expression (*34*). Other macromolecules were conjugated to bacteriophage Q*β* VLP to shield it from immune recognition (*35, 36*). In other directions, PEG was used to tether a fluorescent molecule and folic acid to cowpea mosaic virus for intravital vascular imaging and targeted cargo delivery to cancer cell lines, respectively (*37, 38*).

64 Our model VLP is assembled from 180 copies of *Acinetobacter* phage coat protein AP205
65 (*25*). AP205 VLP is a versatile platform for genetic and/or chemical conjugation of various
66 antigenic molecules thus potentiating a vaccination strategy (*25, 39-41*). We investigated
67 surface crosslinking of AP205 VLP using PEG tethers. To explore different modes of
68 PEGylation, the AP205 VLP was reacted with homobifunctional (leading to surface
69 crosslinking) and monofunctional (leading to simple PEGylation) linkers. We found that
70 surface crosslinking is a viable toolbox that enhances the various stability profiles of VLPs,
71 of which resilience to mechanical agitation, pH and protease stress are related to mucosal
72 applications. Particularly, PEG crosslinking did not shield immune recognition of capsid
73 coat proteins, enhancing vaccine stability without inhibiting immunogenicity.

# 74 Results

75 Surface crosslinked and simply PEGylated VLPs were produced using homobifunctional
76 and monofunctional PEG molecules respectively. The resulting VLPs are named $bPEG_n$-
77 and $mPEG_n$-AP205 VLP where n is the number of PEG monomers. The functional
78 group(s) of the PEG molecules was N-hydroxysuccinimide (NHS) ester which reacts with
79 lysine residues and N-terminus of coat proteins (c.f. **Figure 1**(b)). The sequence of AP205
80 monomer and the details of the PEG molecules are presented in **S1**. We note that in the
81 conditions used, the crosslinking was at single VLP level, and we did not observe
82 aggregation between the particles (**S2**). Transmission electron microscopy (TEM) showed
83 that the VLPs retained their spherical geometry after the reaction with the linker molecules
84 and no detectable VLP size change for any lengths of PEG crosslinker tested, n = 9–25,
85 was observed (**S3**).

## 86 Crosslinking AP205 VLP capsid using polyethylene glycol (PEG) molecules

87 Investigations with mass spectrometry and reducing SDS-polyacrylamide gel
88 electrophoresis (SDS PAGE) revealed that AP205 VLP reaction with homobifunctional
89 PEG crosslinkers resulted in PEG-crosslinked AP205 dimers, trimers, and possibly higher
90 oligomers. In the representative SDS PAGE shown in **Figure 1**(c), in the lanes associated
91 with $bPEG_n$-AP205 VLPs (n = 9 to 25), bands in the MW range 37–50 kDa (marked with
92 purple arrows/circles) correspond to PEG-crosslinked AP205 dimers, and bands in MW
93 range 50–75 kDa (marked with orange arrows/pentagons) correspond to PEG-crosslinked
94 AP205 trimers. Using nano ultra-performance liquid chromatography coupled to mass
95 spectroscopy, it was found that lysine (K) residues K4 and K61 and K4 and K94 were

96 involved in the crosslinking reaction (**Table S4-7**). In **Figure 1**(d), a schematic of PEG
97 linkages between individual AP205 monomers near the three-fold axis of symmetry is
98 shown. Using coordinates from the cryo-electron microscopy reconstruction of the AP205
99 VLP (5LQP) in Visual Molecular Dynamics (VMD) (*41, 42*), the N-N interatomic distances
100 in K4–K61 linkage were estimated to be 1.8 nm and in K4–K94 linkage to be 1.6 nm and
101 2.4 nm. Calculation of end-to-end probability distributions of $PEG_9$, $PEG_{17}$ and $PEG_{25}$
102 linker molecules using worm-like chain model are shown in **Figure 1**(d) (*43*). The
103 calculated extension lengths are consistent with the interatomic distances. Additional
104 details regarding the conjugation stoichiometry, mass spectroscopy and SDS PAGE are
105 found in **S2**, **S4** and **S5**, respectively.

106 **Enhanced colloidal and enzymatic stability of surface-crosslinked AP205 VLPs**

107 VLPs are potentially interesting scaffolds for the oral or intranasal delivery of biomolecules,
108 requiring stability in pH-varying environments and in the presence of high concentrations
109 of proteases (*1, 2, 12*). Therefore, increasing their stability in the complex mucosal
110 environment is of high translational relevance.

111 Experiments using dynamic light scattering (DLS) showed that native VLP was stable at
112 pH 7.4 but aggregated at pH 2.0–6.0 (**Fig. S6-1**). PEG-crosslinking increased the stability
113 of VLP down to pH ~ 4.0 (**Fig. S6-2**). We then tested the enzymatic stability of PEG-
114 crosslinked VLPs in pig and mouse gastric fluids. In PBS, an incubation time of 2 h (or
115 longer) at 37°C did not affect the stability or electrophoretic mobility of the VLPs (*25*)
116 (**Figure 1**(e)). In pig gastric fluid, which had a pH of 3.0 and high protease concentration,
117 PEG-crosslinked VLPs, namely $bPEG_9$-AP205 VLP, $bPEG_{17}$-AP205 VLP, and $bPEG_{25}$-
118 AP205 VLP, showed improved stability after 5 min of incubation, i.e., a band, marked with
119 arrow, remained at the expected MW, with fewer breakdown products than the unmodified
120 VLP. At the later time points of 30 min, 1 h and 2 h, the intact portion was disintegrated,
121 and signs of aggregation and accumulation of material in the wells of the gel appeared.
122 Interestingly, the PEGylated but not crosslinked VLP, namely $mPEG_{25}$-AP205 VLP,
123 showed a similar behavior to native VLP and disintegrated in as little as 5 min. This
124 observation indicates that PEG-crosslinking VLP capsid, but not PEGylation per se, is a
125 viable approach to overcome the susceptibility of VLPs to colloidal and enzymatic
126 instability.

127 Experiments in pig gastric fluid at pH 4.7 corroborated the stabilizing effect of PEG-
128 crosslinking, but not simple PEGylation, in the presence of proteases (**Fig. S7-1**). At this
129 pH, the PEG-crosslinked VLPs were stable at all time points. In pig gastric fluid at pH 5.5,
130 all VLPs were found to be stable over 1 h of incubation (**Fig. S7-2**). Incubation in mouse
131 gastric fluid at pH 4.6 presented a similar behavior where the PEG-crosslinked VLPs
132 appeared to be more stable compared to the naked and PEGylated but not crosslinked
133 VLP (**Fig. S7-3**).

134

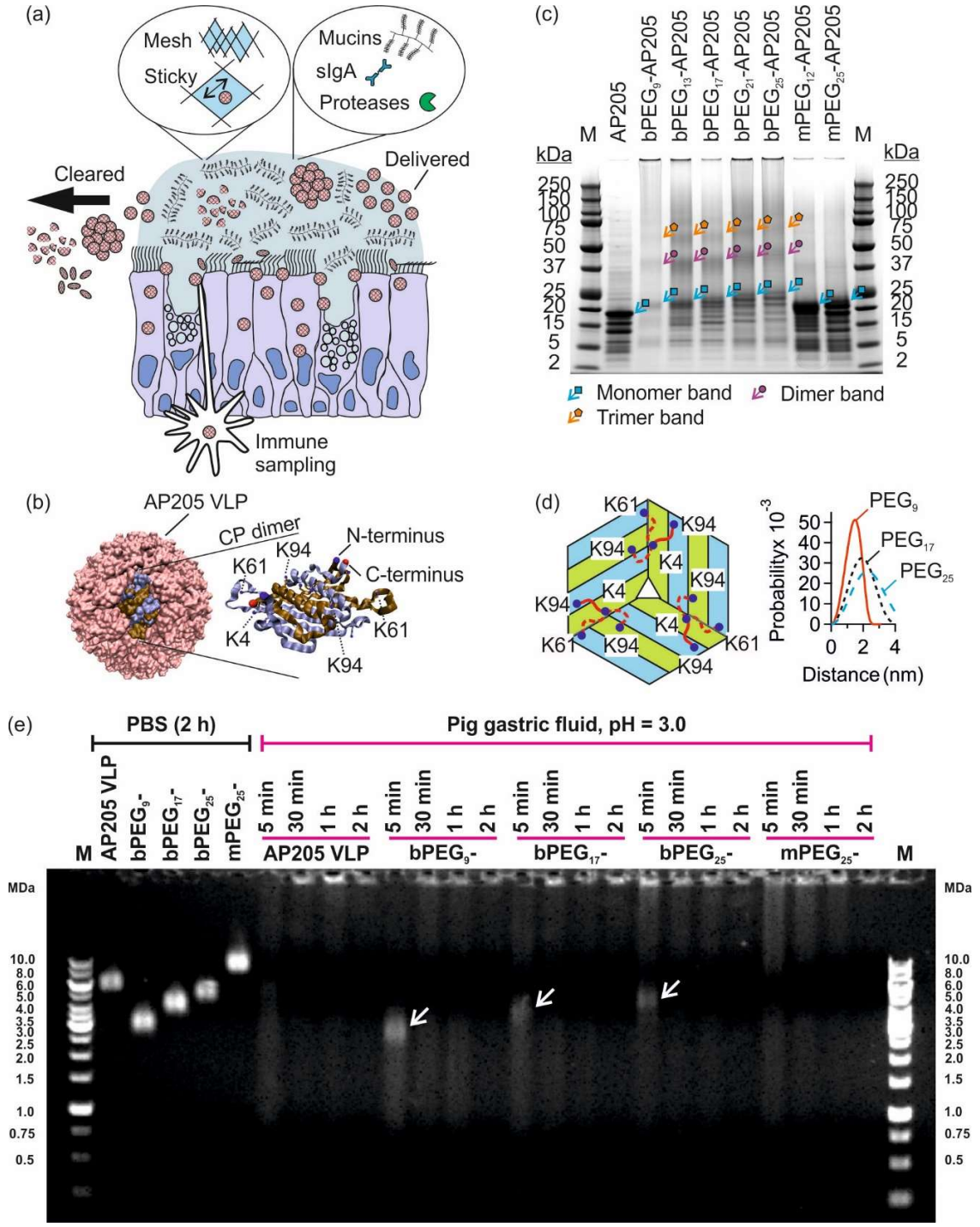


**Figure 1: Susceptibility of virus-like particles (VLPs) to mucosal factors, and their capsid stabilization by means of surface crosslinking using macromolecule tethers.** (a) VLPs are exposed to physical and chemical challenges on mucosal surfaces. (b) Schematic of AP205 VLP and schematic of one coat protein (CP) dimer (*41*). The N-terminus (blue) of one monomer, the C-terminus (red) of the other monomer, together with several lysine residues are marked. (c) Reducing SDS polyacrylamide gel electrophoresis

142 of native, PEG-crosslinked (bPEG$_n$-, n = 9–25), and PEGylated but not crosslinked AP205
143 VLPs (mPEG$_n$-, n = 12 or 25). M is PageRuler Plus Prestained Protein Ladder. The
144 monomer region is marked with cyan arrows/squares, dimer region with purple
145 arrows/circles and trimer region with orange arrows/pentagons. (d) Schematic of AP205
146 CP arrangement near three-fold axis of symmetry and the assignment of lysine residues
147 K4, K61 and K94 that participate in crosslinking reaction. In the schematic, 3 dimers are
148 shown with their monomers colored in blue and green. Only one tether (red coil), that is
149 either of the two of K4–K94 possibilities or the one of K4–K61 possibility, can occur. The
150 end-to-end probability distributions of bPEG$_n$ tethers (n = 9, 17 and 25) calculated from an
151 analytical worm-like chain model (*43*). (e) Agarose gel electrophoresis of AP205 VLP,
152 bPEG$_9$-AP205 VLP, bPEG$_{17}$-AP205 VLP, bPEG$_{25}$-AP205 VLP and mPEG$_{25}$-AP205 VLP
153 in PBS and in pig gastric fluid (pH 3.0), respectively on the left and right of the gel.
154 Incubation times varied between 5 min, 30 min, 1 hour and 2 hours at 37°C. Arrows at
155 time point 5 min indicate persistent PEG-crosslinked AP205 VLPs in gastric fluid. M stands
156 for marker.
157

158 **Enhanced stiffness of surface-crosslinked AP205 VLPs**

159 Susceptibility to mechanical stress sets a limit on potential applications of VLPs in various
160 indications. This occurs during interactions with cells, e.g. during endocytosis or antigen
161 presentation to B cells, or when exposed to mucus or fecal flow (*44-50*). Therefore, we
162 examined the nanomechanical properties of native and PEG-crosslinked VLPs using
163 atomic force microscopy (AFM) force-indentation spectroscopy.

164 The schematic of AFM measurements is depicted in **Figure 2**(a) and details are provided
165 in the methods section. The example shown in **Figure 2**(b) depicts a single representative
166 AP205 VLP for which the height prior to indentation ($H_{\mathrm{i}}$) and after indentation ($H_{\mathrm{f}}$) were
167 evaluated. **Figure 2**(c) shows the heights distributions of AP205 VLP with the respective
168 average values. The force versus indentation distance ($F-\delta$) curve was used to
169 calculate the stiffness, and the force versus indentation time ($F-t$) curve to calculate
170 the strain rate. An example of these curves for the same VLP (**Figure 2**(b)) is shown in
171 **Figure 2**(d). The linear part of the response was used to calculate the stiffness, $k = dF/d\delta$
172 , the total indentation, $\delta = \Delta F/k$, and the indentation force rate $\dot{F} = dF/dt$, which was
173 converted to strain rate via $\gamma = \dot{F}/k\delta$. After an initial linear response, the VLP yielded at a
174 threshold force/indentation. The histograms of maximal force and indentation (indent.) of
175 AP205 VLP together with the average values of these parameters are shown in **Figure**
176 **2**(e). The physical significance of these parameters is that at a force (or indentation) higher
177 than the average maximal force (or indentation), yield occurs which significantly reduces
178 the original stiffness of the VLP (*16-18, 22-25*). The histograms of stiffness and strain rate

179 of AP205 VLP together with the average values of these parameters are shown in **Figure**
180 **2**(f) and (g), respectively. For this VLP, we previously showed that the standard linear solid
181 model (SLSM, **Figure 2**(h)) interprets the stiffness as a function of the strain rate (*25*). We
182 found that at a strain rate < 100 1/s, the overall mechanical response is governed by $k_0$
183 in SLSM. We retrieved a good agreement between the current evaluation of AP205
184 stiffness (47±15 pN/nm) with the previous one (53±23 pN/nm) at low strain rates.

185

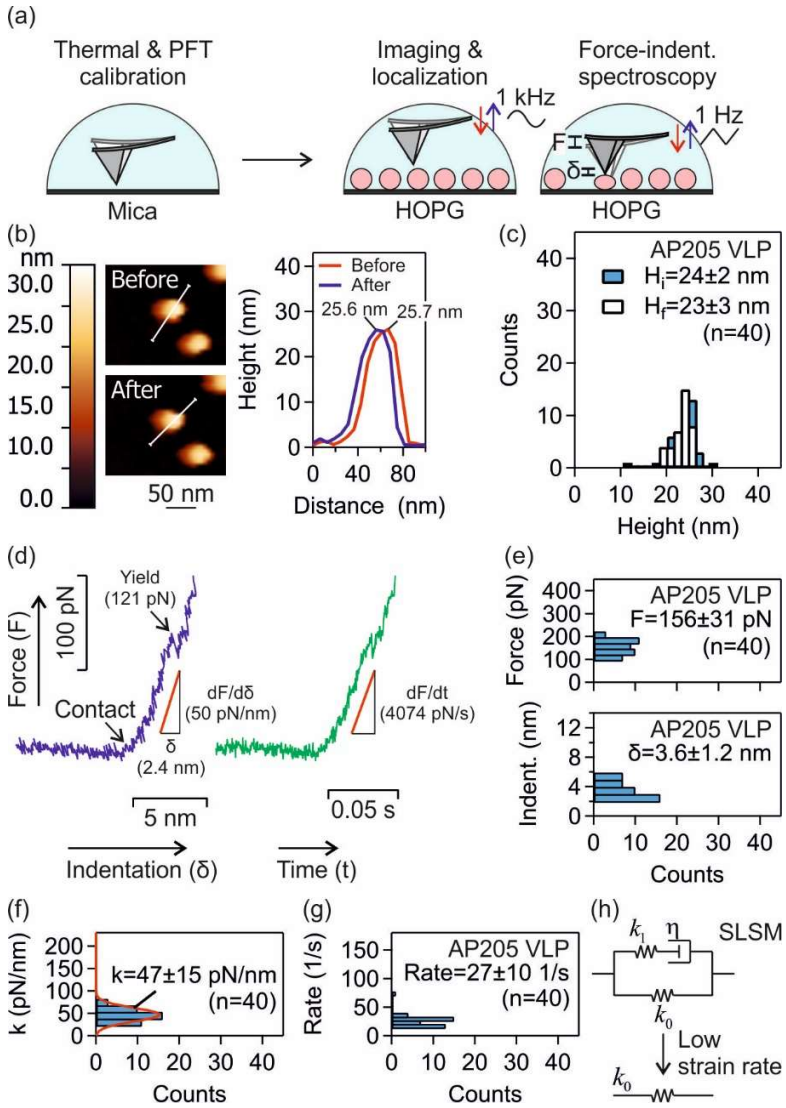


186

187 **Figure 2: Mechanical properties of AP205 VLP investigated using AFM force-**
188 **indentation spectroscopy.** (a) Schematic of AFM calibration on freshly cleaved mica,
189 and force-indentation spectroscopy of HOPG-immobilized VLPs. Single VLPs were
190 localized using PeakForce tapping imaging (base tapping rate of 1 kHz) prior to force

measurements using normal ramp at base approach-retraction rate at 1 Hz. (b) Example of height evaluation for a single AP205 VLP before and after force application. (c) Height distributions of AP205 VLP before and after force measurements. (d) Example of force-indentation distance and force-indentation time curves for AP205 VLP. The linear regime of force-indentation distance response was used to calculate the stiffness. In the same range, a linear fit to force-indentation time response gave the indentation force rate. (e, f and g) Histograms of maximal force and indentation (indent.) (e), stiffness (f) and strain rate (g) of AP205 VLP. Mean ± standard deviation is reported. The number (n) of AP205 VLPs in repeat measurements is indicated. (h) Standard linear solid model (SLSM). At low strain rates, there is no contribution from friction (or rate dependent resistance) to indentation.

Similarly, the mechanical properties of PEG-crosslinked VLPs, namely $bPEG_9$-AP205 VLP, $bPEG_{17}$-AP205 VLP, $bPEG_{25}$-AP205 VLP were evaluated, and the results are shown in **Figure 3**. The initial heights and the heights after a single indentation showed similarity among the native and PEG-crosslinked VLPs. The distributions of maximal force and indentation (indent.) however showed variations compared to native VLP. The average maximal force was found to be higher and accordingly the average maximal indentation lower compared to native VLP. The increased (decreased) maximal force (indentation) of PEG-crosslinked VLPs indicated reduced susceptibility to mechanical agitation. Accordingly, the average stiffness for these VLPs was also higher by a factor of 1.3 to 2.0 than the stiffness of native VLP at similar range of strain rate.

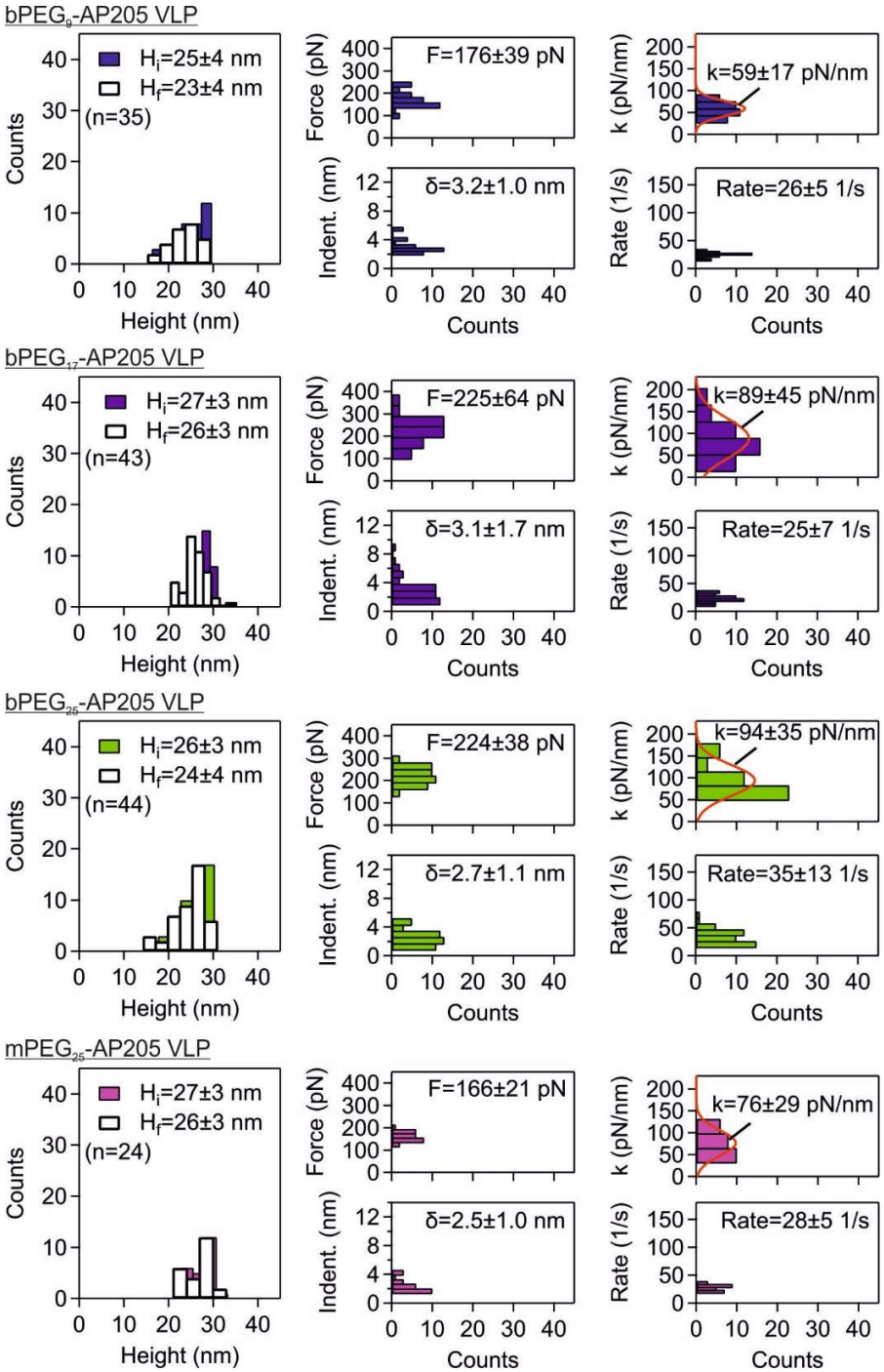


**Figure 3: Enhanced strength and stiffness of PEG-crosslinked AP205 VLPs.** Mechanical properties of PEG-crosslinked AP205 VLPs, namely $bPEG_9$-AP205 VLP, $bPEG_{17}$-AP205 VLP and $bPEG_{25}$-AP205 VLP, and PEGylated but not crosslinked $mPEG_{25}$-AP205 VLP investigated using AFM force-indentation spectroscopy. Distributions of height before and after indentation, maximal force/indentation in linear response regime, and stiffness/strain rate are shown together with mean ± standard deviation. The number (n) of VLPs in repeat measurements is indicated.

222

223 We then evaluated capsid size and shell thickness using small angle X-ray scattering
224 (SAXS). The X-ray scattering spectra of the native and PEGylated VLPs together with fits
225 to spherical core-shell form factor are shown in **Figure 4**(a). In each case, we found a
226 good agreement based on the low values for the fitting error ( $\chi^2$ ). In the summary panel
227 in **Figure 4**(b), it is shown that the diameter ( $D$ ) and shell thickness ( $h$ ) of VLP increased
228 after PEGylation. In addition, while the VLP diameter remained somewhat constant
229 between the different lengths of PEG tethers, the shell thickness increased with PEG
230 length and had its highest value for the PEGylated but not crosslinked VLP. Subsequent
231 to these evaluations, the elastic modulus was calculated from the relation $E = Dk/2h^2$ ,
232 **Figure 4**(b) (*51, 52*). The elastic moduli remained somewhat constant ~ 90 MPa among
233 the native and PEG-crosslinked VLPs. This observation can potentially be explained as
234 follows. In nanoindentation experiments, the shell compression and bending moduli
235 contribute to an effective elastic modulus $E$ (*52-54*). Tethered PEG molecules disfavor
236 bending because it results in chain stretching, therefore increasing the bending modulus.
237 Reduction in coat protein positive charges after PEG conjugation reduces the inter-atomic
238 repulsion during compression, therefore decreasing the compression modulus. The higher
239 stiffness of PEG-crosslinked VLPs compared to native VLP is therefore associated with
240 an increase in the shell thickness, as well as stretching the PEG molecules (*55*). The effect
241 of chain stretching became evident where the PEGylated but not crosslinked VLP, namely
242 $mPEG_{25}$-AP205 VLP, was investigated. This VLP showed a lower elastic modulus and
243 stiffness compared to its PEG-crosslinked counterpart, namely $bPEG_{25}$-AP205 VLP
244 (**Figure 3** and **Figure 4**).

245

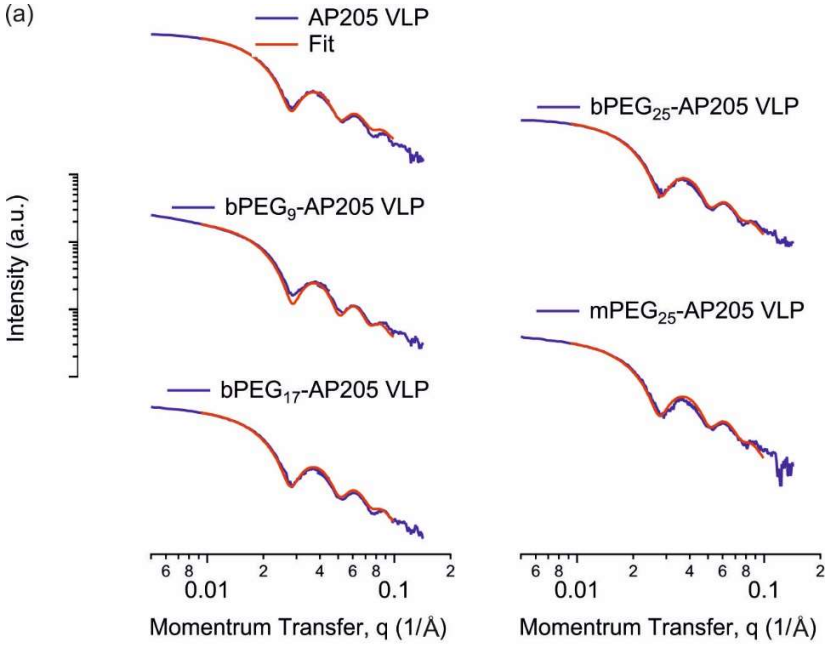


(b)

| VLP entry | Stiffness (pN/nm) | Diameter (nm) | Shell thickness (nm) | Elastic modulus (MPa) |
|---|---|---|---|---|
| AP205 | 47±15 | 27.6 | 2.7 | 89±28 |
| $bPEG_9$-AP205 | 59±17 | 28.8 | 3.2 | 83±24 |
| $bPEG_{17}$-AP205 | 89±45 | 28.5 | 3.6 | 98±49 |
| $bPEG_{25}$-AP205 | 94±35 | 28.4 | 4.0 | 83±31 |
| $mPEG_{25}$-AP205 | 76±29 | 28.8 | 4.4 | 57±22 |

**Figure 4: Geometrical and mechanical parameters of native and PEGylated AP205 VLPs.** (a) Small angle X-ray scattering (SAXS) spectra of AP205, $bPEG_9$-AP205, $bPEG_{17}$-AP205, $bPEG_{25}$-AP205 and $mPEG_{25}$-AP205 VLPs, together with fits to spherical core-shell form factor. (b) Summary panel of the geometrical and mechanical properties of the VLPs.

## Surface-crosslinking does not restrict mucus translocation of AP205 VLP

A major feature of intestinal and respiratory sites, where VLP application is relevant, is the production of mucus. Mucus is an adhesive and viscoelastic gel that covers the epithelium and functions to trap and dispose of foreign objects. In the airways, mucus is constantly pushed out via mucociliary clearance (*56, 57*). We used *in vitro* 3D human nasal epithelial tissues to investigate the effect of PEG-crosslinking on translocation across flowing mucus. The tissues were characterized as having fully differentiated mucus producing goblet cells, ciliated cells with motile cilia, as well as other cells of normal human nasal epithelial tissue. The schematic of the experiments is shown in **Figure 5**(a). On delivery of fluorescently labelled VLPs from the apical side, the VLPs translocated through mucus

263 by diffusion and simultaneously transported in flowing mucus in the direction of mucociliary
264 clearance to edges of the tissue. The lateral distribution and vertical translocation were
265 monitored using laser scanning confocal microscopy (LSCM). In **Figure 5**(b),
266 representative examples of mean fluorescence intensity (MFI) variation with height
267 collected in the center, [0, 0] mm, prior to VLP delivery (VLP-) and after the delivery of
268 mPEG$_{25}$-AP205 VLP$^{GelRed}$ (VLP+) are shown. In the former case, the location of maximum
269 MFI was at the height level of the semipermeable membrane which was assigned to 0 µm.
270 After VLP delivery, the maximum of MFI shifted to a higher height value (about 40 µm)
271 while the peak associated with semipermeable membrane was observable. The MFI vs
272 height spectra were normalized (norm. MFI) by the MFI values at height = 0 µm, **Figure**
273 **5**(b). The normalized MFI spectrum of VLP- was then subtracted from that of VLP+ to give
274 the net MFI spectrum. The net MFI spectra from the center, [0, 0] mm, together with
275 spectra at positions [-1, 0] mm, [+1, 0] mm, [0, -1] mm and [0, +1] mm, are shown in **Figure**
276 **5**(c). These spectra provided information about the height location of VLP deposition and
277 the net value of MFI at those deposition heights, which corresponded to the translocated
278 amount of VLPs. In all experiments, it was ensured via bright field microscopy that the cilia
279 were beating before and after VLP delivery using stablished procedures (*58*).

280 A typical deposition height and translocated amount of native and PEG-crosslinked VLPs
281 are shown in **Figure 5**(d) and (e). A similar deposition height between these VLPs was
282 expected as tissues from the same donor (tissue 3) were used. Furthermore, as shown in
283 **Figure 5**(e), similar translocated amounts between the native and PEG-crosslinked VLPs
284 were obtained. This observation indicated that PEG-crosslinking did not restrict nor
285 increased VLP translocation through mucus. These results were consistent on other
286 tissues (**S8**). We then investigated the translocation behavior of PEGylated but not
287 crosslinked VLP, namely mPEG$_{25}$-AP205 VLP$^{GelRed}$. We found that mPEG$_{25}$-AP205
288 VLP$^{GelRed}$ showed a similar deposition height (**Figure 5**(d)), however it had an increased
289 translocation amount which exceeded native VLP by two folds (**Figure 5**(e)). Particularly
290 as compared to bPEG$_{25}$-AP205 VLP, this result indicated a higher mucus permeability of
291 the mPEG$_{25}$-AP205 VLP construct. Consistent with previous reports (*59-61*), a potential
292 explanation is an effective steric hinderance interactions with mucin glycoproteins from
293 one-end conjugated PEGs.

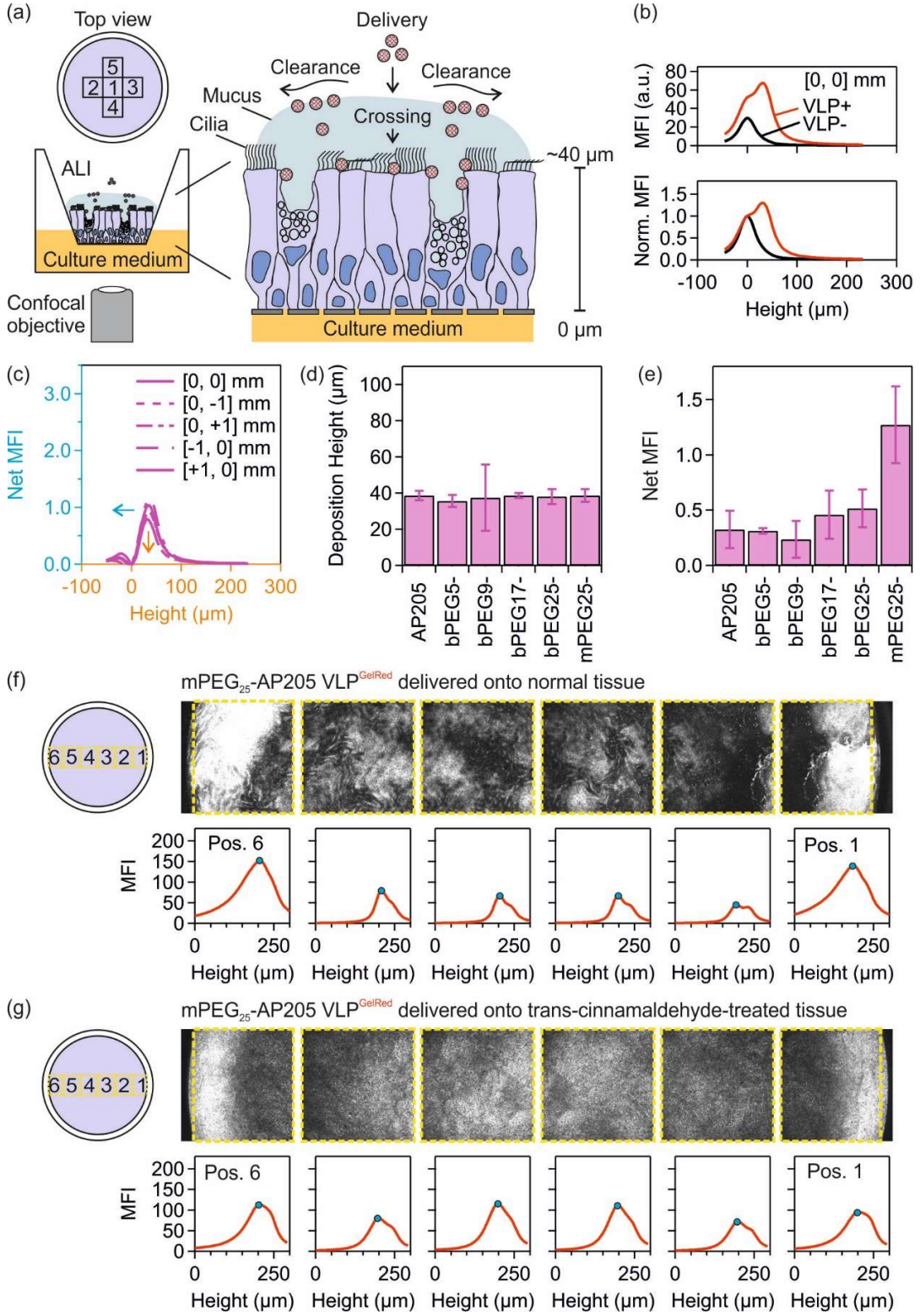


**Figure 5: Translocation through mucus of AP205 VLPs in *in vitro* 3D human nasal epithelial tissues.** (a) Schematic of *in vitro* nasal epithelial tissue and delivery of

297 fluorescently-labelled virus-like particles (VLPs) from the apical side. Using laser scanning
298 confocal microscopy (objective lens 10x, N.A. 0.3), the lateral distribution and vertical
299 translocation through mucus of VLPs were monitored at several position 1: [0, 0] mm, 2:
300 [-1, 0] mm, 3: [+1, 0] mm, 4: [0, -1] mm and 5: [0, +1] mm. (b) Mean fluorescence intensity
301 (MFI) and normalized MFI (norm. MFI) variation with height collected in the center of tissue
302 3. MFI and norm. MFI spectra prior to VLP delivery, VLP-, and after the delivery of
303 $mPEG_{25}$-AP205 $VLP^{GelRed}$, VLP+, are shown. The height of semipermeable membrane is
304 set to 0 µm. (c) Subtracted (or net) MFI spectra on five positions showing the height
305 location of VLP deposition and the net MFI. (d, e) The deposition height (d) and the net
306 MFI corresponding to the translocated amount of VLPs (c) of native and PEGylated VLPs
307 on tissue 3. (f) Delivery of $mPEG_{25}$-AP205 $VLP^{GelRed}$ to tissue 3. (g) Delivery of $mPEG_{25}$-
308 AP205 $VLP^{GelRed}$ to trans-cinnamaldehyde-treated tissue 3. The yellow box denotes the
309 area of mean fluorescence intensity (MFI) calculation and blue circle the height location
310 of VLP deposition. In these figures, height starts from above the air-liquid interface (ALI)
311 and increases in the direction of cell layer to below the semipermeable membrane. The
312 height of the semipermeable membrane is approximatively 250 µm. The individual
313 confocal images on lateral positions 1 to 6 were taken at a fixed height distance from the
314 semipermeable membrane.
315

316 We then investigated the effect of outward-swirling mucociliary clearance on the
317 deposition of VLPs across the tissue (*62*). $mPEG_{25}$-AP205 $VLP^{GelRed}$ was delivered in
318 normal tissue condition or when the tissue was treated with trans-cinnamaldehyde.
319 Analysis of the lateral distribution of deposited VLPs across the tissue (positions 1 to 6)
320 under normal conditions (**Figure 5**(f)) showed that a noticeable portion of VLP was cleared
321 to the edge of the plastic insert in flowing mucus while a portion translocated similar to the
322 observations already discussed. However, the lateral distribution of deposited VLPs was
323 more uniform across the tissue when ciliary beating was stopped (**Figure 5**(g)). Additional
324 examples of the deposited VLP distribution when ciliary beating was inhibited are shown
325 in **SI 9**.

326

327 **Compatibility of PEG-crosslinking with vaccine function**

328 A major application of VLPs is in mucosal delivery of vaccine antigens. We therefore
329 investigated if PEG-crosslinking may interfere with this function by measuring antibody
330 induction against coat protein in native and PEG-crosslinked VLPs in a subcutaneous
331 vaccination model using C57BL/6J specific pathogen free (SPF) mice, i.e. a setting where
332 vaccine stability is thought not to be a major limitation on performance. Accordingly,
333 subcutaneous injections of VLPs without additional adjuvant were performed on Day 0
334 and 10. The mice were sacrificed on Day 20 and anti-AP205 serum IgG titers detected

using enzyme-linked immunosorbent assay (ELISA). The serum antibody titers against AP205 coat protein are shown in **Figure 6**(a). As expected, native VLP was immunogenic, and we easily detected specific serum IgG antibodies against AP205 coat protein (*39, 40*). Surprisingly, PEG-crosslinking, or simple PEGylation of VLP did not shield immune activation against the coat protein; rather, specific antibody induction was increased. Potentially several mechanisms could be involved, and one cannot make a direct correlation with stiffness. Antibody induction against the PEG coating was also investigated. Consistent with the strong adjuvanticity of VLPs (*63*), the anti-PEG ELISA in **Figure 6**(b) showed that the injection of PEGylated VLPs, compared to the negative control, i.e., native VLP, resulted in anti-PEG IgG induction. Furthermore, the anti-PEG IgG titers seemed to increase with the size of two-end conjugated PEG crosslinker, i.e., to be higher in the order $bPEG_9$-AP205 VLP < $bPEG_{17}$-AP205 VLP < $bPEG_{25}$-AP205 VLP.

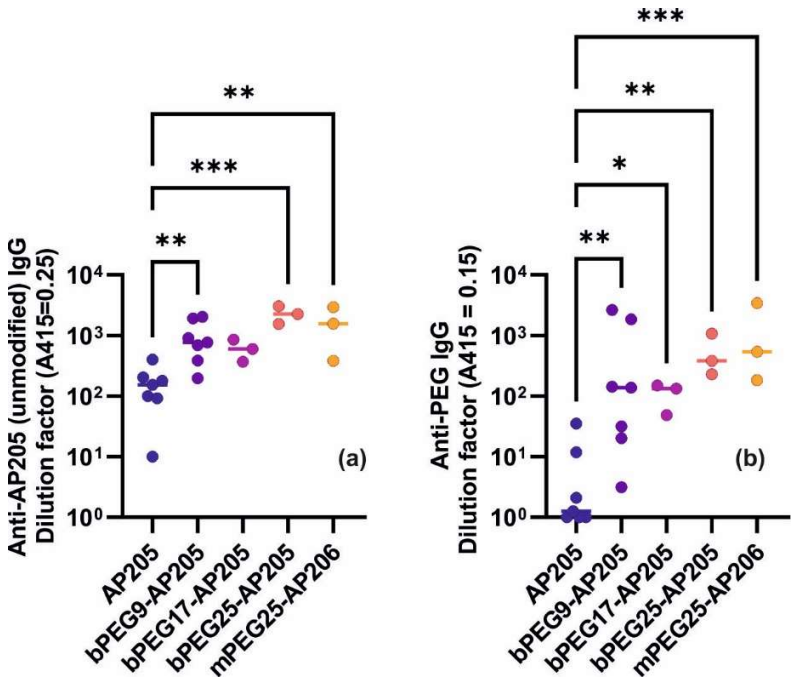


**Figure 6: Immune activation by PEG-crosslinked AP205 VLPs.** C57BL/6J SPF mice were subcutaneously injected with native (n = 7), PEG-crosslinked (n = 13), or PEGylated but not crosslinked (n = 3) AP205 VLPs on Day 0 and Day 10 and sacrificed on Day 20. Serum antibody (IgG) titers against (a) AP205 coat protein, and (b) PEG was measured by ELISA. Statistical significance was determined by ordinary one-way ANOVA with Dunnett's multiple comparisons test, with a single pooled variance on log-normalized data (*P = 0.0332; ***P = 0.0021; ***P = 0.0002).

357 # Discussion

358 VLPs have similar physical characteristics to their viruses of origin, including size,
359 proteinaceous core-shell structure, and patchy surface charge distribution, and like viruses
360 are prone to aggregation, disintegration, and sticking to surfaces rendering them non-
361 functional (*64*). Enhancing the stability of VLPs is therefore justified in future developments
362 of VLP biotechnology, particularly for mucosal applications. We investigated surface
363 crosslinking as a means to achieve the latter. We found that it increased the colloidal
364 stability of VLPs at low pH (**S6**) as it protected them against proteases. Specifically, while
365 the native AP205 VLP disintegrated in pig gastric fluid at pH 3.0 and 4.7 in less than 5
366 min, the surface-crosslinked VLPs presented a longer lifetime in the same fluids (**Figure**
367 **1** and **S7**). Susceptibility to mechanical agitation was introduced as another limiting factor
368 to VLP mucosal application. Using different force probing techniques, the endocytosis
369 "pulling" force exerted by a cell onto a virus, B cell antigen extraction, and the force of cilia
370 agitation were measured to vary between a few to hundreds of pN (*44-50*). Although this
371 force range is generally below the yield force values of VLPs, when applied repeatedly as
372 they do *in vivo*, they can disintegrate the capsids due to fatigue (*16-18, 22-25*). Therefore,
373 it is also logical to mechanically reinforce VLPs and surface-crosslinking was found to
374 increase the stiffness and strength of AP205 VLP (**Figure 2** and **Figure 4**).

375 Mucosal applications of VLPs are faced with other physiological challenges, namely
376 translocation through a thick mucus layer. Particularly in the airways, the mucus is subject
377 to mucociliary clearance which further reduces VLP translocation efficiency by pushing
378 the mucus out of the airways (*56*). Experiments using *in vitro* 3D human nasal epithelial
379 tissues showed an effective translocation of native and surface-crosslinked AP205 VLPs,
380 while mucociliary clearance transported mucus at a speed of about 40–200 μm/s
381 (measured at 1–3 mm from the tissue center, (*62, 65*)) in a swirling rotation to the edges
382 of the tissue (**Figure 5**). Is mucus a poor barrier to VLPs of a size below about 100 nm,
383 including AP205 VLP (27.6 nm), and VLPs of human papilloma virus and Norwalk virus
384 (respectively, 55 nm and 38 nm, (*66*))? Considering viruses that infect mucosal surfaces,
385 including polio (28 nm), hepatitis B (43 nm), adenoviruses (60–90 nm), rotavirus (75 nm),
386 human immunodeficiency virus (120 nm) and herpes simplex virus (180 nm) (*67*), one
387 may conclude that small viruses are capable of deeply penetrating the mucus. This is
388 expected when the pore size of mucus gel (≥ 50 nm) exceeds the size of these viruses.
389 However, penetration is further facilitated by the patchy surface charge distribution on

390 capsids (*66, 67*). Therefore, structural point mutations as well as macromolecule
391 entanglement with mucin glycoproteins can alter the diffusion of VLPs in mucus (*68*).

392 Finally, our results suggest that the material properties of VLPs are relevant variables that
393 should be further investigated to improve mucosal applications. As schematically shown
394 in **Figure 1**(a), both chemical, enzymatic, and physical stresses can affect the efficacy of
395 VLP delivery to the respiratory or intestinal mucosal epithelium. In this work, crosslinking
396 of multiple surface sites was shown to be a promising approach to improve and extend
397 the range of VLP mucosal functions by increasing resistance to degradation and improving
398 physical stability. These modifications actually slightly enhance even parenteral
399 vaccination indicating that the tethers did not shield the coat proteins from immune
400 recognition, and that increase biochemical stability may also be beneficial systemically
401 (**Figure 6**). PEG immunogenicity is currently an unwanted side-effect that may be
402 overcome with use of alternative crosslinkers in the future. Critically, our work
403 demonstrates the potential to improve the current VLP system to generate structures
404 compatible with overall enhanced functionality, strength, stability and immunogenicity at
405 mucosal surfaces.

406

# 407 Materials and Methods

## 408 Experimental Design

409 Surface crosslinking of virus-like particle (VLP) capsids using polyethylene glycol (PEG)
410 tethers was investigated against physiological challenges to assess its performance on
411 mucosal surfaces. The model native VLP was derived from the coat protein of
412 Acinetobacter phage, namely AP205 VLP. PEG tethers included two-end functional PEG
413 molecules of various molecular weights. The PEG-crosslinked AP205 VLPs were initially
414 evaluated in terms of the reaction products and the sites of PEG conjugation to reactive
415 surface sites (using a combination of dynamic light scattering, transmission electron
416 microscopy, reducing SDS-polyacrylamide gel electrophoresis, electrospray ionization
417 mass spectroscopy and nano ultra-performance liquid chromatography-MS) and then
418 investigated for the aggregation behavior against pH (using dynamic light scattering),
419 disintegration against digestive enzymes from pig and mouse gastric fluid (using agarose
420 gel electrophoresis), resistance to mechanical force (using atomic force microscopy), and

421 penetration in mucus in the presence of motile cilia and mucociliary clearance (using *in*
422 *vitro* 3D human nasal tissues).
423

424 **Production of AP205 VLP**

425 The biosynthesis of AP205 VLP is reported in details in our previous study (*25*). Briefly, it
426 includes the expression of recombinant AP205 coat proteins in bacterial cytoplasm which
427 then self-assemble into AP205 VLPs. After the expression of VLP, a series of steps
428 consisting of bacterial lysis, digestion of RNA and DNA contaminants, and extraction of
429 lipids were performed prior to precipitation and dialysis against PBS to produce purified
430 AP205 VLPs. Plasmids were generated by custom DNA synthesis (Twist Bioscience, San
431 Francisco, CA, USA) of the expression cassettes and cloning into the pRSFDuet-1
432 (Novagen) backbone between the PfoI and BshTI restriction sites. Sequences of the
433 plasmids are available via the ETH-Zürich research collection at
434 https://doi.org/10.3929/ethz-b-000556182. The sequence of AP205 monomer and the
435 description of plasmid are reported in **S1**.

436 **PEGylation of AP205 VLP**

437 The functional group on the extremities of homobifunctional PEG crosslinker molecules
438 ($bPEG_n$, n = 5 to 25) and on one extremity of monofunctional PEG molecules ($mPEG_n$, n
439 = 12 and 25) was NHS-ester which is reactive to primary amine of lysine residues and N-
440 terminus of AP205 coat proteins. Reactions with native AP205 VLP proceeded at 1–100x
441 molar ratio of crosslinker molecule to AP205 monomer (
442 $\text{molar ratio} = [\text{functional moleucle}]/[\text{AP205 CP}]$ ). The PEG molecule was dissolved in
443 anhydrous and molecular sieves dried dimethyl sulfoxide (DMSO, Sigma-Aldrich) to a
444 concentration of 100 mM. An appropriate amount was then added to AP205 VLP
445 suspension at 4 mg/ml in PBS. The reaction was left for 24 h at 4°C. Then after, it was
446 quenched by adding Tris•HCl (Trizma® base, Sigma-Aldrich, and hydrochloric acid 37%,
447 VWR) at 20–50 mM and incubating for 15 min. Unreacted PEG molecules and Tris were
448 removed using Zeba Spin Desalting Column (ThermoFisher) with molecular weight cut-off
449 at 7 kDa. Other reactive molecules including $BS^3$ and Sulfo-NHS were used similarly;
450 however, they were initially dissolved to 100 mM in PBS. A summary of the physical
451 properties of these molecules is provided in **S1**.

452 **Fluorescent staining of VLPs**

453 We defined a mixing ratio $x = \text{mass of stain}/\text{mass of VLP} = 10^{-2}$, and a final stained VLP
454 concentration equal to 5.3 mg/ml. (To calculate the mass of stain, we assumed 10,000x
455 to correspond to 10 mg/ml.) GelRed® (10,000x in water, biotium) or SYBRGold™ (10,000x
456 in DMSO) were used and staining proceeded for 30 min. To remove unbound dye, the
457 solution of stained VLP was buffer exchanged with pure PBS using Zeba™ Spin Desalting
458 Columns (7,000 MWCO, ThermoFisher). We note that since the columns contained
459 sodium azide, it was important to buffer the column with pure PBS prior to cleaning the
460 stained VLP solution. The stained VLP solution was finally filtered using 0.2 µm centrifuge
461 filters (Corning® Costar® Spin-X® centrifuge tube filters) to remove possible aggregates.
462 The intensity of stained VLPs was monitored over time using laser scanning confocal
463 microscopy and showed no noticeable reduction over a course of at least two weeks.

464 **Transmission electron microscopy (TEM)**

465 4 µl VLP solution (0.1 mg/ml) was deposited on glow-discharged (45 sec, 25 mA, negative
466 charge) carbon-coated grids (Ted Pella) for 1-5 min, after which the excess liquid was
467 removed using filter paper. Then the grid was rinsed with 5 µl of PBS to remove loosely
468 bound VLPs. Subsequently, 3 µl of 2% uranyl acetate was applied and immediately
469 removed with filter paper prior to a second treatment with 3 µl of 2% uranyl acetate for 20
470 sec. Excess liquid was again collected using filter paper and the grid was let dry at room
471 temperature (RT). Data acquisition was performed using a Morgani transmission electron
472 microscope operating at 100 kV acceleration voltage.

473 **Electrospray ionization mass spectrometry (ESI-MS)**

474 ESI-MS was acquired on a Synapt G2-Si quadrupole time-of-flight spectrometer (Waters,
475 UK) with a capillary voltage of 3 V, a cone voltage of 50 V and a source temperature of
476 100°C. VLPs at a concentration of 1 mg/ml were reduced by dithiothreitol (DTT) at a final
477 concentration of 50 mM. The reduction was performed for 1 h at RT and at pH 8. The
478 samples were acidified with 1% formic acid (Thermo, USA), desalted using C4 Zip Tips
479 (Millipore, USA) and analyzed in methanol:2-propanol:0.2 % formic acid (30:20:50). The
480 solutions were infused through a fused silica capillary (ID 75 µm) at a flow rate of 1 µl/min
481 and sprayed through Pico Tips (ID 30 µm). The last were obtained from New Objective
482 (Woburn, MA, USA). Recorded m/z data were deconvoluted using the MaxEnt1 software
483 (Waters, UK) with a resolution of the output mass of 0.5 Da per channel and a Uniform
484 Gaussian Damage Model at the half-height of 0.5 Da.

485 **Nano ultra-performance liquid chromatography-MS (nanoUPLC-MS/MS)**

486 NanoUPLC-MS/MS was acquired on Thermo FUSION mass spectrometer (Thermo,
487 Germany) coupled to a nano-M-class UPLC system (Waters). $BPEG_9$-AP205 VLP at a
488 concentration of 1 mg/ml was digested by incubating 3 µl of the sample with 42 µl of 25
489 mM ammonium bicarbonate (pH 8.5) and 1 µl of TCEP (100 mM) for 1 h at 37°C. Reduced
490 protein was incubated with 2 µl chloroacetamide (500 mM) for 1 h at 37°C. Then after, 5
491 µl trypsin (0.1 µg/µl in 10 mM HCl) was added and the solution further incubated overnight
492 at 37°C. When needed the pH was adjusted to pH 8. At the end of this procedure, the
493 sample was dried using SpeedVac. Digested and dried sample was dissolved in 20 µl
494 $ddH_2O$ with 0.1% formic acid and diluted 5 times before transferring to autosampler vials.
495 Peptides were resuspended in 2.5% acetonitrile with 0.1% formic acid and loaded onto a
496 nanoEase M/Z Symmetry C18 (75 µm × 20 mm, 100 Å, 3 µm particle size) and separated
497 on a nanoEase M/Z HSS C18 T3 (75 µm × 150 mm, 130 Å, 1.7 µm particle size) at a
498 constant flow rate of 300 nl/min, with a column temperature of 50°C and a linear gradient
499 of 2−32% acetonitrile/0.1% formic acid in 79 min, and then 32-45% acetonitrile/0.1%
500 formic acid in 10 min, followed by a sharp increase to 98% acetonitrile in 2 min and then
501 held at 98% for another 10 min. Mass spectrometer was operated under data-dependent
502 acquisition (DDA), one scan cycle comprised of a full scan MS survey spectrum, followed
503 by up to 12 sequential higher-collisional energy (HCD) MS/MS on the most intense signals
504 above a threshold of 1e4. Full-scan MS spectra (600–2000 m/z) were acquired in the FT-
505 Orbitrap at a resolution of 70,000 at 400 m/z, while HCD MS/MS spectra were recorded
506 in the FT-Orbitrap at a resolution of 35,000 at 400 m/z. HCD was performed with a target
507 value of 1e5 and normalization collision energy 25 NCE (normalize collisional energy) was
508 applied. Auto-gain control (AGC) target values were 5e5 for full Fourier transform (FT)
509 MS. For all experiments, dynamic exclusion was used with a single repeat count, 15 s
510 repeat duration, and 30 s exclusion duration. The acquired MS data were processed for
511 identification using the Byonic search engine (PMI). The spectra were searched against
512 AP205 VLP sequence and AP205 VLP sequence with E. *Coli* database. The following
513 modifications were included: (a) variable modifications, namely oxidation at N-terminus
514 methionine and carbamidomethylation at cysteine (C), and (b) user-defined modifications,
515 namely 478.2565 ($C_{22}O_{11}H_{38}$) was set for $PEG_9$-crosslinked peptides and 496.2565
516 ($C_{22}O_{12}H_{40}$) for one-end $PEG_9$ conjugation at a lysine residue or N-Terminus. In this
517 analysis, the raw data were analyzed by two software, PMI Byonic search engine and SIM

518 1.5.5.3 (Spectrum identification machine) (*69*). In addition, two FastA databases with and
519 without starting methionine were used to confirm the N-terminus.

520 **SDS-polyacrylamide gel electrophoresis (SDS-PAGE)**

521 Denaturing and reducing SDS-PAGE was carried out in 13% Tricine gels. Samples of 3
522 µg of VLP were denatured and reduced in Laemmli sample buffer at 95°C for 5 min prior
523 to electrophoresis. Proteins were visualized by Coomassie staining.

524 **Dynamic light scattering (DLS)**

525 DLS was performed at a fixed angle of 173° by averaging 3 runs of 30-s long each using
526 Zetasizer Nano (Malvern Panalytical). The time correlation function of scattered intensity
527 was analyzed by the cumulant as well as CONTIN methods. The VLP concentration was
528 initially adjusted to 0.1 mg/ml in filtered PBS prior to measurements.

529 **Gastric fluid collection**

530 Pig gastric content was collected from the stomach of conventionally reared, outbred pigs
531 with different genetic contributions of French-Swiss Landrace and Swiss Large White.
532 Total gastric content was collected. Mouse gastric content was obtained by collecting total
533 stomach content from several specific opportunistic pathogen-free (SPF) C57BL/6J WT
534 mice. The gastric content from several mice was pooled to have sufficient volume. Pig or
535 mouse gastric content was centrifuged for 5 min at 16000 rpm to separate the non-
536 digested food particles. After the collection of supernatant (gastric fluid), it was filtered
537 using 0.22 µm sterile filter and the pH measured using a laboratory pH-meter.

538 **Agarose gel electrophoresis**

539 VLPs from 1 mg/ml preparation were diluted 1:10 in pig or mouse gastric fluid and
540 incubated for 5 min, 30 min, 1 h and 1.5 or 2 h at 37°C. After each incubation, the samples
541 were immediately placed on ice. Native agarose gel electrophoresis of PBS- or gastric
542 fluid-treated VLPs was carried out in 0.6% agarose in TAE buffer (40 mM Tris, 0.1% acetic
543 acid, 1 mM EDTA) with 0.5 µg/ml of ethidium bromide for visualization. Samples of 5 µg
544 VLP were electrophoresed at 120 Volts for 1 h, then imaged on a UV transilluminator.

545 **Atomic force microscopy (AFM)**

546 The schematic of AFM measurements is shown in **Figure 2**(a). After an initial calibration,
547 which also included the calibration of PeakForce tapping mode, on freshly cleaved mica,

548 the tip was brought in proximity to VLPs immobilized at a concentration of 5 µg/ml on
549 Highly Oriented Pyrolytic Graphite (HOPG, Ted Pella, Inc.) The calibrated parameters
550 included stiffness (59.4–82.0 pN/nm) using thermal method and optical lever sensitivity
551 using cantilever–mica contact region (*70*), and drive3 amplitude sensitivity. During the
552 transport of cantilever from mica to HOPG, the cantilever remained wet, and the laser spot
553 was checked to remain on the same spot. The calibration values were re-measured on
554 mica at the end of the measurements to detect any noticeable variation to the calibrated
555 parameters. Single VLPs were localized on HOPG by imaging in PeakForce tapping mode
556 (peak force 50 pN, tapping frequency 1 kHz, amplitude 30 nm). Generally, images of
557 individual VLPs were acquired at a scan rate of 0.7 Hz with 200×200 or 500×500 $nm^2$ scan
558 size and a resolution of 64 points per line, leading to a pixel size of 3 nm. After localization,
559 we used "Point & Shoot" function (NanoScope, Bruker) to place the AFM tip on the apex
560 of selected VLPs before applying indentation using Ramp mode. The VLPs were indented
561 up to a threshold force value of 400 pN at a preset frequency of 1 Hz, which resulted in an
562 indentation force rate of about (4–9)×$10^3$ pN/s. Indented particles were imaged again in
563 PeakForce tapping to detect signs of degradation, drift, or displacement due to tip lateral
564 forces. The height of individual VLPs before ($H_i$) and after ($H_f$) indentation were
565 calculated by placing a trace line over the particles on images previously flattened using
566 Gwyddion 2.47 (*71*). For stiffness evaluation, we proceeded as follows: deflection versus
567 piezo displacement was converted to force versus tip separation using protocols written
568 in Igor Pro (Wavemetrics). Fit to force versus indentation distance ($F-\delta$) curve in the
569 linear response part of the tip–VLP contact region gave the stiffness ($k = dF/d\delta$) and the
570 indentation ($\delta = \Delta F/k$). The fit was performed in the force range $50\,\mathrm{pN} \le F \le 250\,\mathrm{pN}$, and
571 only those VLPs with indentation range $2.0 \le \delta \le 6.0\,\mathrm{nm}$ were selected for averaging. Only
572 one indentation per VLP was used for the evaluations. The indentation force rate ($\dot{F}$) was
573 calculated from a linear fit to the force versus indentation time ($F-t$) curve in the same
574 region were the stiffness of VLP was calculated. Strain rate was then calculated from the
575 relation $\dot{\gamma} = \dot{F}/k\delta$. Average stiffness was calculated from at least duplicate independent
576 VLP preparations. UV-ozone (Novascan) cleaned AC40 BioLever Mini cantilevers
577 (Bruker) were used. Dimension FastScan (Bruker) was used for imaging and force
578 spectroscopy.

579 **Small angle X-ray scattering (SAXS)**

580 We used a Xeuss 2.0 (Xenocs, France) instrument with a microfocused X-ray source at
581 the Laboratory Léon Brillouin (LLB NIMBE CEA Saclay). The Cu Kα radiation ($\lambda_{Cu\ K\alpha}$ =
582 1.5418 Å), and the data were collected by a 2D Pilatus 1 M detector (Dectris, Switzerland).
583 The scattering vector $q = 4\pi/\lambda \sin(\theta/2)$, with $\theta$ being the scattering angle was calibrated
584 using silver behenate. Data were collected and azimuthally averaged to produce
585 unidimensional intensity versus $q$, with $q$ interval of 0.005 to 0.1 $Å^{-1}$. The measurements
586 were performed at 25°C. The scattering intensity was collected for 2600 s. The intensity
587 was corrected for sample thickness, transmission, and acquisition time. The modelling of
588 the integrated data was performed with a core-shell form factor, and a hard sphere
589 structure factor, when needed, using the SasView software.

590 ***In vitro* 3D human nasal epithelial tissue**

591 *In vitro* human nasal epithelial tissues from single donors (MucilAir™) were obtained from
592 Epithelix (Switzerland). The tissues were maintained according to company's protocols
593 and included tissue 1 from a Caucasian 64-year-old female subject (MD0860), tissue 2
594 from a Caucasian 46-year-old male subject (MD0871) and tissue 3 from a Caucasian 38-
595 year-old male subject (MD0774). The subjects were non-smokers and had no history of
596 respiratory pathology.

597 **Inhibition of mucociliary clearance**

598 Ciliary beating was inhibited using trans-cinnamaldehyde (97%, C80687, Sigma-Aldrich).
599 Trans-cinnamaldehyde was dissolved in MucilAir™ culture medium to a concentration of
600 30 mM. To improve solubility, freshly prepared solution was sonicated for 15 min and the
601 solution was kept at 37°C prior to filling the basal channel of MucilAir™ monodonor nasal
602 epithelial tissue. After 20 min of incubation, the ciliary beating stopped, and no recovery
603 was observed for up to 2 h (*72*).

604 **Delivery of VLPs to *in vitro* 3D human nasal epithelial tissue**

605 Tissues were incubated in a humidified-$CO_2$ chamber at 37°C. After a period of
606 equilibration 0.5–1 h, 5 µl of VLP solution (5.3 mg/ml) was delivered from the apical side.
607 The delivery was onto the center of the tissue.

608 **Laser scanning confocal microscopy (LSCM)**

609 Lateral distribution and vertical translocation of fluorescently labelled VLPs through mucus
610 were then monitored using laser scanning confocal microscopy (LSCM, Leica SP5
611 confocal microscope). We used a 10x objective lens with N.A. 0.3. Excitation wavelength
612 $\lambda_{ex} = 488\ \mathrm{nm}$ was used for SYBRGold™- stained VLPs and Salmonella vaccine with
613 detection wavelength $\lambda_{em} = 500 - 590\ \mathrm{nm}$. $\lambda_{ex} = 514\ \mathrm{nm}$ was used for GelRed®-stained
614 VLPs with $\lambda_{em} = 550 - 650\ \mathrm{nm}$. The channel spectral detection was set to HyD (Gain equal
615 to 100). The mean fluorescence intensity (MFI) variation with height was collected in the
616 center [0, 0] mm, and on positions [-1, 0] mm, [+1, 0] mm, [0, -1] mm and [0, +1] mm prior
617 to, during and after VLP delivery. Leica LAS AF software was used for saving the images.
618 Analysis was performed using ImageJ.

619 **Mice**

620 All animal experiments were performed in accordance with Swiss Federal regulations
621 approved by the Commission for Animal Experimentation of the Kanton Zurich (license
622 ZH009/2021, Kantonales Veterinäramt Zürich, Switzerland). SPF C57BL/6J WT mice
623 were used in all experiments. Mice were bred and housed in individually ventilated cages
624 with a 12 h light/dark cycle in the ETH Phenomics Center (EPIC, RCHCI), ETH Zürich,
625 and were fed a standard chow diet. All mice included in experiments were 7 weeks or
626 older and objectively healthy as determined by routine health checks. Wherever possible
627 an equal number of males and females was used in each experimental group.

628 **Subcutaneous injection**

629 50 µg of VLP in 100 µl of PBS was subcutaneously injected into the loose skin over the
630 interscapular area of C57BL/6J SPF mice on Day 0 and Day 10. The mice were
631 euthanized on Day 20. Blood was collected by cardiac puncture, and serum separated by
632 spinning 1.1 ml serum gel tubes (Sarstedt) at 10,000 g for 5 min at 20°C in a conventional
633 table-top centrifuge, and heat-inactivated for 30 min at 56°C.

634 **Enzyme-linked immunosorbent assay (ELISA) for detection of anti-AP205 IgG**
635 **response**

636 50 µl of AP205 VLP solution (5 µg/ml) was pipetted into an appropriate number of wells of
637 ELISA plates (4 Nunc MaxiSorp flat bottom 96-well plates) and the VLP allowed to adsorb
638 overnight at 4°C. The wells were washed three times with wash buffer (0.05% Tween 20
639 in PBS) and blotted. The wells were blocked using 150 µl of blocking buffer (2% bovine

640 serum albumin in PBS) for 1.5 h at RT. Subsequently, the wells were washed five times
641 with wash buffer and blotted. Mouse sera were diluted ten times in blocking buffer, and
642 sequentially in 1:3 dilution steps added to the wells of ELISA plates. The plates were
643 incubated for 2 h at RT to allow the binding of serum IgG to AP205 proteins. Goat anti-
644 mouse IgG-HRP (Sigma) was diluted a thousand-fold in blocking buffer, and 50 µl of
645 solution added to the wells and incubated for 1 h at RT. The wells were washed five times
646 using wash buffer and blotted. Finally, 150 µl of freshly prepared substrate solution
647 (consisting of 0.1 M $NaH_2PO_4$ (substrate buffer), 2,2'-azino-bis(3-ethylbenzothiazoline-6-
648 sulfonic acid (1–2 mg per 10 ml of substrate buffer), and $H_2O_2$ (10 µl per 10 ml)) was added
649 to each well. The plate was incubated in the dark for 40 min. On Tecan (Tecan Infinite 200
650 PRO microplate reader), absorbance was measured at 415 nm. The reference wavelength
651 for the subtraction of background signal was set to 480 nm.

652 **Enzyme-linked immunosorbent assay (ELISA) for detection of anti-PEG IgG**
653 **response**

654 Mouse sera were diluted ten times in PEG dilution buffer (PEGD50-1, Life Diagnostics,
655 Inc.), and sequentially in 1:3 dilution steps added to the wells of PEG-BSA coated ELISA
656 plates (PBSA20PL, Life Diagnostics, Inc.) The plates were incubated for 2 h at RT to allow
657 antibody binding. The wells were washed five times with 300 µl PEG wash buffer
658 (PEGW50-20, Life Diagnostics, Inc.) and blotted. Goat anti-mouse IgG-HRP (AP124P,
659 Sigma-Aldrich) was diluted a thousand-fold in PEG dilution buffer and 100 µl of this
660 solution was added to each well with an incubation of 1 h at RT. The wells were washed
661 and blotted again. Finally, 150 µl of freshly prepared substrate solution was added to each
662 well. The plates were incubated in the dark for 40 min. On Tecan (Tecan Infinite 200 PRO
663 microplate reader), absorbance was measured at 415 nm. The reference wavelength for
664 the subtraction of background signal was set to 480 nm.

665 **Statistical Analysis**

666 AFM and LSCM results were expressed as mean ± standard deviation analyzed by Igor
667 Pro from WaveMetrics. *In vivo* mouse vaccination results were assessed using ordinary
668 one-way ANOVA with Dunnett's multiple comparisons test using GraphPad Prism
669 (*P = 0.0332; ***P = 0.0021; ***P = 0.0002).
670

671

# Acknowledgments

We acknowledge the contributions from Till Germerdonk in DLS measurements, and discussions with Patrick Zueblin. We also acknowledge the time for SAXS measurements provided by the Leon Brillouin Laboratory (LLB), and the support of Fabrice Cousin.

**Funding**

European Research Council (ERC) Grant number 865730 (MR, YT, AA and ES)

Swiss National Science Foundation, Switzerland, rant number IZSEZ0_212991 (MR)

Swiss National Science Foundation, Switzerland, grant numbers 40B2-0_180953 (ES)

Swiss National Science Foundation, Switzerland, grant numbers 310030_185128 (ES)

National Center for Competence in Research in Microbiomes, Switzerland (ES)

Botnar Research Centre for Child Health Multi-investigator project “Microbiota Engineering for Child Health” (ES)

Gebert Rüf Microbials, grant number GR073_17 (ES)

Cystic Fibrosis Trust UK SRC 016 (PC, JK, RF)

EU ITN PhyMot (EC)


**Author contributions**

Conceptualization: MR

Methodology: MR, PC, RM, ES

Investigation: MR, AA, SG, VL, TK, YT, WLB, EC, SC, CWL, JK

Writing—original draft: MR

Writing—review & editing: All authors

Funding acquisition: MR, PC, ES

**Competing interests**

Authors declare that they have no competing interests.

**Data and materials availability**

All data used in the analyses are available without limitation from the first author.

## Supplementary Materials

Further information regarding the Materials and Methods are provided in Supplementary Materials (**S**).

# References


1. Y. H. Chung, H. Cai, N. F. Steinmetz, Viral nanoparticles for drug delivery, imaging, immunotherapy, and theranostic applications. *Advanced Drug Delivery Reviews* **156**, 214-235 (2020).
2. H. Tariq, S. Batool, S. Asif, M. Ali, B. H. Abbasi, Virus-Like Particles: Revolutionary Platforms for Developing Vaccines Against Emerging Infectious Diseases. *Frontiers in Microbiology* **12**, (2022).
3. H. Hu, N. F. Steinmetz, Development of a Virus-Like Particle-Based Anti-HER2 Breast Cancer Vaccine. *Cancers* **13**, (2021).
4. D. Yin, S. Ling, D. Wang, Y. Dai, H. Jiang, X. Zhou, S. R. Paludan, J. Hong, Y. Cai, Targeting herpes simplex virus with CRISPR-Cas9 cures herpetic stromal keratitis in mice. *Nat Biotechnol* **39**, 567-577 (2021).
5. S. Banskota, A. Raguram, S. Suh, S. W. Du, J. R. Davis, E. H. Choi, X. Wang, S. C. Nielsen, G. A. Newby, P. B. Randolph, M. J. Osborn, K. Musunuru, K. Palczewski, D. R. Liu, Engineered virus-like particles for efficient in vivo delivery of therapeutic proteins. *Cell* **185**, 250-265.e216 (2022).
6. J. Mianné, A. Nasri, C. N. Van, C. Bourguignon, M. Fieldès, E. Ahmed, C. Duthoit, N. Martin, H. Parrinello, A. Louis, A. Iché, R. Gayon, F. Samain, L. Lamouroux, P. Bouillé, A. Bourdin, S. Assou, J. De Vos, CRISPR/Cas9-mediated gene knockout and interallelic gene conversion in human induced pluripotent stem cells using non-integrative bacteriophage-chimeric retrovirus-like particles. *BMC Biology* **20**, 8 (2022).
7. C. Sakai, K. Hosokawa, T. Watanabe, Y. Suzuki, T. Nakano, K. Ueda, M. Fujimuro, Human hepatitis B virus-derived virus-like particle as a drug and DNA delivery carrier. *Biochemical and Biophysical Research Communications* **581**, 103-109 (2021).
8. E. C. Thuenemann, D. H. T. Le, G. P. Lomonossoff, N. F. Steinmetz, Bluetongue Virus Particles as Nanoreactors for Enzyme Delivery and Cancer Therapy. *Mol Pharm* **18**, 1150-1156 (2021).
9. S. Panthi, P. T. Schmitt, F. J. Lorenz, B. A. Stanfield, A. P. Schmitt, Paramyxovirus-Like Particles as Protein Delivery Vehicles. *J Virol* **95**, e0103021 (2021).
10. A. Shahrivarkevishahi, M. A. Luzuriaga, F. C. Herbert, A. C. Tumac, O. R. Brohlin, Y. H. Wijesundara, A. V. Adlooru, C. Benjamin, H. Lee, P. Parsamian, J. Gadhvi, N. J. De Nisco, J. J. Gassensmith, PhotothermalPhage: A Virus-Based Photothermal Therapeutic Agent. *J Am Chem Soc* **143**, 16428-16438 (2021).
11. H. Lee, A. Shahrivarkevishahi, J. L. Lumata, M. A. Luzuriaga, L. M. Hagge, C. E. Benjamin, O. R. Brohlin, C. R. Parish, H. R. Firouzi, S. O. Nielsen, L. L. Lumata, J. J. Gassensmith, Supramolecular and biomacromolecular enhancement of metal-free magnetic resonance imaging contrast agents. *Chemical Science* **11**, 2045-2050 (2020).
12. A. Armanious, M. Radiom, R. Mezzenga, Recent Experimental Advances in Probing the Colloidal Properties of Viruses. *Current Opinion in Colloid & Interface Science*, 101703 (2023).
13. V. Sankar, V. Hearnden, K. Hull, D. V. Juras, M. Greenberg, A. Kerr, P. Lockhart, L. Patton, S. Porter, M. Thornhill, Local drug delivery for oral mucosal diseases: challenges and opportunities. *Oral Diseases* **17**, 73-84 (2011).
14. J. O. Morales, K. R. Fathe, A. Brunaugh, S. Ferrati, S. Li, M. Montenegro-Nicolini, Z. Mousavikhamene, J. T. McConville, M. R. Prausnitz, H. D. C. Smyth, Challenges and Future Prospects for the Delivery of Biologics: Oral Mucosal, Pulmonary, and Transdermal Routes. *The AAPS Journal* **19**, 652-668 (2017).
15. S. Hua, Advances in Oral Drug Delivery for Regional Targeting in the Gastrointestinal Tract - Influence of Physiological, Pathophysiological and Pharmaceutical Factors. *Frontiers in Pharmacology* **11**, (2020).
16. I. L. Ivanovska, P. J. d. Pablo, B. Ibarra, G. Sgalari, F. C. MacKintosh, J. L. Carrascosa, C. F. Schmidt, G. J. L. Wuite, Bacteriophage capsids: Tough nanoshells with complex elastic properties. *Proceedings of the National Academy of Sciences* **101**, 7600-7605 (2004).

17. J. P. Michel, I. L. Ivanovska, M. M. Gibbons, W. S. Klug, C. M. Knobler, G. J. L. Wuite, C. F. Schmidt, Nanoindentation studies of full and empty viral capsids and the effects of capsid protein mutations on elasticity and strength. *Proceedings of the National Academy of Sciences* **103**, 6184-6189 (2006).
18. N. Kol, M. Gladnikoff, D. Barlam, R. Z. Shneck, A. Rein, I. Rousso, Mechanical Properties of Murine Leukemia Virus Particles: Effect of Maturation. *Biophysical Journal* **91**, 767-774 (2006).
19. C. Carrasco, A. Carreira, I. A. T. Schaap, P. A. Serena, J. Gómez-Herrero, M. G. Mateu, P. J. d. Pablo, DNA-mediated anisotropic mechanical reinforcement of a virus. *Proceedings of the National Academy of Sciences* **103**, 13706-13711 (2006).
20. N. Kol, Y. Shi, M. Tsvitov, D. Barlam, R. Z. Shneck, M. S. Kay, I. Rousso, A Stiffness Switch in Human Immunodeficiency Virus. *Biophysical Journal* **92**, 1777-1783 (2007).
21. I. Ivanovska, G. Wuite, B. Jönsson, A. Evilevitch, Internal DNA pressure modifies stability of WT phage. *Proceedings of the National Academy of Sciences* **104**, 9603-9608 (2007).
22. A. Llauró, D. Luque, E. Edwards, B. L. Trus, J. Avera, D. Reguera, T. Douglas, P. J. d. Pablo, J. R. Castón, Cargo–shell and cargo–cargo couplings govern the mechanics of artificially loaded virus-derived cages. *Nanoscale* **8**, 9328-9336 (2016).
23. A. Ortega-Esteban, G. N. Condezo, A. J. Pérez-Berná, M. Chillón, S. J. Flint, D. Reguera, C. San Martín, P. J. de Pablo, Mechanics of Viral Chromatin Reveals the Pressurization of Human Adenovirus. *ACS Nano* **9**, 10826-10833 (2015).
24. M. Jiménez-Zaragoza, M. P. L. Yubero, E. Martín-Forero, J. R. Castón, D. Reguera, D. Luque, P. J. de Pablo, J. M. Rodríguez, Biophysical properties of single rotavirus particles account for the functions of protein shells in a multilayered virus. *eLife* **7**, e37295 (2018).
25. M. Radiom, T. Keys, Y. Turgay, A. Ali, S. Peret, S. Chesnov, V. Lutz-Bueno, E. Slack, R. Mezzenga, Mechanical tuning of virus-like particles. *Journal of Colloid and Interface Science* **634**, 963-971 (2023).
26. C. Zeng, L. Scott, A. Malyutin, R. Zandi, P. Van der Schoot, B. Dragnea, Virus Mechanics under Molecular Crowding. *The Journal of Physical Chemistry B* **125**, 1790-1798 (2021).
27. M. Cantero, D. Carlero, F. J. Chichón, J. Martín-Benito, P. J. De Pablo, Monitoring SARS-CoV-2 Surrogate TGEV Individual Virions Structure Survival under Harsh Physicochemical Environments. *Cells* **11**, (2022).
28. C. R. O'Riordan, A. Lachapelle, C. Delgado, V. Parkes, S. C. Wadsworth, A. E. Smith, G. E. Francis, PEGylation of adenovirus with retention of infectivity and protection from neutralizing antibody in vitro and in vivo. *Hum Gene Ther* **10**, 1349-1358 (1999).
29. M. A. Croyle, N. Chirmule, Y. Zhang, J. M. Wilson, PEGylation of E1-deleted adenovirus vectors allows significant gene expression on readministration to liver. *Hum Gene Ther* **13**, 1887-1900 (2002).
30. M. A. Croyle, N. Chirmule, Y. Zhang, J. M. Wilson, "Stealth" adenoviruses blunt cell-mediated and humoral immune responses against the virus and allow for significant gene expression upon readministration in the lung. *J Virol* **75**, 4792-4801 (2001).
31. E. A. Weaver, M. A. Barry, Effects of shielding adenoviral vectors with polyethylene glycol on vector-specific and vaccine-mediated immune responses. *Hum Gene Ther* **19**, 1369-1382 (2008).
32. T. Shimizu, M. Ichihara, Y. Yoshioka, T. Ishida, S. Nakagawa, H. Kiwada, Intravenous administration of polyethylene glycol-coated (PEGylated) proteins and PEGylated adenovirus elicits an anti-PEG immunoglobulin M response. *Biol Pharm Bull* **35**, 1336-1342 (2012).
33. K. L. Lee, S. Shukla, M. Wu, N. R. Ayat, C. E. El Sanadi, A. M. Wen, J. F. Edelbrock, J. K. Pokorski, U. Commandeur, G. R. Dubyak, N. F. Steinmetz, Stealth filaments: Polymer chain length and conformation affect the in vivo fate of PEGylated potato virus X. *Acta Biomater* **19**, 166-179 (2015).
34. Y. Eto, Y. Yoshioka, T. Ishida, X. Yao, T. Morishige, S. Narimatsu, H. Mizuguchi, Y. Mukai, N. Okada, H. Kiwada, S. Nakagawa, Optimized PEGylated adenovirus vector reduces the anti-vector humoral immune response against adenovirus and induces a therapeutic effect against metastatic lung cancer. *Biol Pharm Bull* **33**, 1540-1544 (2010).

35. P. W. Lee, S. A. Isarov, J. D. Wallat, S. K. Molugu, S. Shukla, J. E. Sun, J. Zhang, Y. Zheng, M. Lucius Dougherty, D. Konkolewicz, P. L. Stewart, N. F. Steinmetz, M. J. Hore, J. K. Pokorski, Polymer Structure and Conformation Alter the Antigenicity of Virus-like Particle-Polymer Conjugates. *J Am Chem Soc* **139**, 3312-3315 (2017).
36. S. N. Crooke, J. Zheng, M. S. Ganewatta, S. M. Guldberg, T. M. Reineke, M. G. Finn, Immunological Properties of Protein–Polymer Nanoparticles. *ACS Applied Bio Materials* **2**, 93-103 (2019).
37. J. D. Lewis, G. Destito, A. Zijlstra, M. J. Gonzalez, J. P. Quigley, M. Manchester, H. Stuhlmann, Viral nanoparticles as tools for intravital vascular imaging. *Nature Medicine* **12**, 354-360 (2006).
38. G. Destito, R. Yeh, C. S. Rae, M. G. Finn, M. Manchester, Folic Acid-Mediated Targeting of Cowpea Mosaic Virus Particles to Tumor Cells. *Chemistry & Biology* **14**, 1152-1162 (2007).
39. A. C. Tissot, R. Renhofa, N. Schmitz, I. Cielens, E. Meijerink, V. Ose, G. T. Jennings, P. Saudan, P. Pumpens, M. F. Bachmann, Versatile Virus-Like Particle Carrier for Epitope Based Vaccines. *PLOS ONE* **5**, e9809 (2010).
40. X. Liu, X. Chang, D. Rothen, M. Derveni, P. Krenger, S. Roongta, E. Wright, M. Vogel, K. Tars, M. O. Mohsen, M. F. Bachmann, AP205 VLPs Based on Dimerized Capsid Proteins Accommodate RBM Domain of SARS-CoV-2 and Serve as an Attractive Vaccine Candidate. *Vaccines* **9**, 403 (2021).
41. M. Shishovs, J. Rumnieks, C. Diebolder, K. Jaudzems, L. B. Andreas, J. Stanek, A. Kazaks, S. Kotelovica, I. Akopjana, G. Pintacuda, R. I. Koning, K. Tars, Structure of AP205 Coat Protein Reveals Circular Permutation in ssRNA Bacteriophages. *Journal of Molecular Biology* **428**, 4267-4279 (2016).
42. W. Humphrey, A. Dalke, K. Schulten, VMD: Visual molecular dynamics (http://www.ks.uiuc.edu/Research/vmd/). *Journal of Molecular Graphics* **14**, 33-38 (1996).
43. D. Thirumalai, B. Y. Ha, "Statistical mechanics of semiflexible chains: pA mean field variational approach" in *Theoretical and mathematical models in polymer research,* A. Grosberg, Ed. (Academic Press: San Diego, 1998).
44. Y. Pan, F. Zhang, L. Zhang, S. Liu, M. Cai, Y. Shan, X. Wang, H. Wang, H. Wang, The Process of Wrapping Virus Revealed by a Force Tracing Technique and Simulations. *Advanced Science* **4**, 1600489 (2017).
45. T. Wiegand, M. Fratini, F. Frey, K. Yserentant, Y. Liu, E. Weber, K. Galior, J. Ohmes, F. Braun, D.-P. Herten, S. Boulant, U. S. Schwarz, K. Salaita, E. A. Cavalcanti-Adam, J. P. Spatz, Forces during cellular uptake of viruses and nanoparticles at the ventral side. *Nature Communications* **11**, 32 (2020).
46. Q. Zhang, F. Tian, F. Wang, Z. Guo, M. Cai, H. Xu, H. Wang, G. Yang, X. Shi, Y. Shan, Z. Cui, Entry Dynamics of Single Ebola Virus Revealed by Force Tracing. *ACS Nano* **14**, 7046-7054 (2020).
47. J. Zhang, Y. Huang, M. Sun, T. Song, S. Wan, C. Yang, Y. Song, Mechanosensing view of SARS-CoV-2 infection by a DNA nano-assembly. *Cell Rep Phys Sci* **3**, 101048 (2022).
48. S. Li, Y. Pan, H. Teng, Y. Shan, G. Yang, H. Wang, Revealing the Cell Entry Dynamic Mechanism of Single Rabies Virus Particle. *Chem Res Chin Univ* **38**, 838-842 (2022).
49. K. M. Spillane, P. Tolar, B cell antigen extraction is regulated by physical properties of antigen-presenting cells. *Journal of Cell Biology* **216**, 217-230 (2017).
50. D. B. Hill, V. Swaminathan, A. Estes, J. Cribb, E. T. O'Brien, C. W. Davis, R. Superfine, Force generation and dynamics of individual cilia under external loading. *Biophys J* **98**, 57-66 (2010).
51. M. P. Neubauer, M. Poehlmann, A. Fery, Microcapsule mechanics: From stability to function. *Advances in Colloid and Interface Science* **207**, 65-80 (2014).
52. M. Buenemann, P. Lenz, Elastic properties and mechanical stability of chiral and filled viral capsids. *Physical Review E* **78**, 051924 (2008).
53. L. Menou, Y. C. Salas, L. Lecoq, A. Salvetti, C. F. Moskalenko, M. Castelnovo, Stiffness heterogeneity of small viral capsids. *Physical Review E* **104**, 064408 (2021).

54. M. Buenemann, P. Lenz, Mechanical limits of viral capsids. *Proceedings of the National Academy of Sciences* **104**, 9925-9930 (2007).
55. Z. L. Luo, B. Zhang, H. J. Qian, Z. Y. Lu, S. X. Cui, Effect of the size of solvent molecules on the single-chain mechanics of poly(ethylene glycol): implications on a novel design of a molecular motor. *Nanoscale* **8**, 17820-17827 (2016).
56. R. Bansil, B. S. Turner, The biology of mucus: composition, synthesis and organization. *Advanced Drug Delivery Reviews* **124**, 3-15 (2018).
57. X. M. Bustamante-Marin, L. E. Ostrowski, Cilia and mucociliary clearance. *Cold Spring Harbor perspectives in biology* **9**, (2017).
58. R. Fradique, E. Causa, C. Delahousse, J. Kotar, L. Pinte, L. Vallier, M. Vila-Gonzalez, P. Cicuta, Assessing motile cilia coverage and beat frequency in mammalian in vitro cell culture tissues. *Royal Society Open Science* **10**, 230185 (2023).
59. Y. Y. Wang, S. K. Lai, J. S. Suk, A. Pace, R. Cone, J. Hanes, Addressing the PEG mucoadhesivity paradox to engineer nanoparticles that "slip" through the human mucus barrier. *Angew Chem Int Ed Engl* **47**, 9726-9729 (2008).
60. C. S. Schneider, Q. Xu, N. J. Boylan, J. Chisholm, B. C. Tang, B. S. Schuster, A. Henning, L. M. Ensign, E. Lee, P. Adstamongkonkul, B. W. Simons, S. S. Wang, X. Gong, T. Yu, M. P. Boyle, J. S. Suk, J. Hanes, Nanoparticles that do not adhere to mucus provide uniform and long-lasting drug delivery to airways following inhalation. *Sci Adv* **3**, e1601556 (2017).
61. J. T. Huckaby, S. K. Lai, PEGylation for enhancing nanoparticle diffusion in mucus. *Advanced Drug Delivery Reviews* **124**, 125-139 (2018).
62. M.-K. Khelloufi, E. Loiseau, M. Jaeger, N. Molinari, P. Chanez, D. Gras, A. Viallat, Spatiotemporal organization of cilia drives multiscale mucus swirls in model human bronchial epithelium. *Scientific Reports* **8**, 2447 (2018).
63. L. Klimek, T. Kündig, M. F. Kramer, S. Guethoff, E. Jensen-Jarolim, C. B. Schmidt-Weber, O. Palomares, M. O. Mohsen, T. Jakob, M. Bachmann, Virus-like particles (VLP) in prophylaxis and immunotherapy of allergic diseases. *Allergo Journal International* **27**, 245-255 (2018).
64. A. Armanious, R. Mezzenga, A Roadmap for Building Waterborne Virus Traps. *JACS Au* **2**, 2205-2221 (2022).
65. H. Matsui, B. R. Grubb, R. Tarran, S. H. Randell, J. T. Gatzy, C. W. Davis, R. C. Boucher, Evidence for periciliary liquid layer depletion, not abnormal ion composition, in the pathogenesis of cystic fibrosis airways disease. *Cell* **95**, 1005-1015 (1998).
66. S. S. Olmsted, J. L. Padgett, A. I. Yudin, K. J. Whaley, T. R. Moench, R. A. Cone, Diffusion of Macromolecules and Virus-Like Particles in Human Cervical Mucus. *Biophysical Journal* **81**, 1930-1937 (2001).
67. R. A. Cone, Barrier properties of mucus. *Adv Drug Deliv Rev* **61**, 75-85 (2009).
68. G. A. Duncan, N. Kim, Y. Colon-Cortes, J. Rodriguez, M. Mazur, S. E. Birket, S. M. Rowe, N. E. West, A. Livraghi-Butrico, R. C. Boucher, J. Hanes, G. Aslanidi, J. S. Suk, An Adeno-Associated Viral Vector Capable of Penetrating the Mucus Barrier to Inhaled Gene Therapy. *Mol Ther Methods Clin Dev* **9**, 296-304 (2018).
69. D. B. Lima, T. B. de Lima, T. S. Balbuena, A. G. C. Neves-Ferreira, V. C. Barbosa, F. C. Gozzo, P. C. Carvalho, SIM-XL: A powerful and user-friendly tool for peptide cross-linking analysis. *Journal of Proteomics* **129**, 51-55 (2015).
70. H. J. Butt, B. Cappella, M. Kappl, Force measurements with the atomic force microscope: Technique, interpretation and applications. *Surface Science Reports* **59**, 1-152 (2005).
71. D. Nečas, P. Klapetek, Gwyddion: an open-source software for SPM data analysis. *Open Physics* **10**, 181-188 (2012).
72. P. W. Clapp, K. S. Lavrich, C. A. v. Heusden, E. R. Lazarowski, J. L. Carson, I. Jaspers, Cinnamaldehyde in flavored e-cigarette liquids temporarily suppresses bronchial epithelial cell ciliary motility by dysregulation of mitochondrial function. *American Journal of Physiology-Lung Cellular and Molecular Physiology* **316**, L470-L486 (2019).